# Energy-level structure of Sn³⁺ ions

J. Scheers,[1,2] A. Ryabtsev,[3] A. Borschevsky,[4] J. C. Berengut,[5] K. Haris,[6] R. Schupp,[1] D. Kurilovich,[1,2] F. Torretti,[1,2]
A. Bayerle,[1] E. Eliav,[7] W. Ubachs,[1,2] O. O. Versolato,[1] and R. Hoekstra[1,8,*]

[1]*Advanced Research Center for Nanolithography, Science Park 110, 1098 XG Amsterdam, The Netherlands*
[2]*Department of Physics and Astronomy, and LaserLaB, Vrije Universiteit, De Boelelaan 1081, 1081 HV Amsterdam, The Netherlands*
[3]*Institute of Spectroscopy, Russian Academy of Sciences, Troitsk, Moscow 108840, Russia*
[4]*Van Swinderen Institute, University of Groningen, Nijenborgh 4, 9747 AG Groningen, The Netherlands*
[5]*School of Physics, University of New South Wales, Sydney 2052, Australia*
[6]*Department of Physics, Aligarh Muslim University, Aligarh 202002, India*
[7]*School of Chemistry, Tel Aviv University, 69978 Tel Aviv, Israel*
[8]*Zernike Institute for Advanced Materials, University of Groningen, Nijenborgh 4, 9747 AG Groningen, The Netherlands*

Laser-produced Sn plasma sources are used to generate extreme ultraviolet light in state-of-the-art nanolithography. An ultraviolet and optical spectrum is measured from a droplet-based laser-produced Sn plasma, with a spectrograph covering the range 200–800 nm. This spectrum contains hundreds of spectral lines from lowly charged tin ions $Sn^{1+} - Sn^{4+}$ of which a major fraction was hitherto unidentified. We present and identify a selected class of lines belonging to the quasi-one-electron, Ag-like ([Kr]$4d^{10} nl$ electronic configuration), $Sn^{3+}$ ion, linking the optical lines to a specific charge state by means of a masking technique. These line identifications are made with iterative guidance from COWAN code calculations. Of the 53 lines attributed to $Sn^{3+}$, some 20 were identified from previously known energy levels, and 33 lines are used to determine previously unknown level energies of 13 electronic configurations, i.e., $7p$, $(7, 8)d$, $(5, 6)f$, $(6-8)g$, $(6-8)h$, $(7, 8)i$. The consistency of the level energy determination is verified by the quantum-defect scaling procedure. The ionization limit of $Sn^{3+}$ is confirmed and refined to 328 908.4 cm⁻¹, with an uncertainty of 2.1 cm⁻¹. The relativistic Fock-space coupled-cluster (FSCC) calculations of the measured level energies are generally in good agreement with experiment but fail to reproduce the anomalous behavior of the $5d\,^2D$ and $nf\,^2F$ terms. By combining the strengths of the FSCC calculations, COWAN code calculations, and configuration interaction many-body perturbation theory, this behavior is shown to arise from interactions with doubly excited configurations.

## I. INTRODUCTION

Emission of light by neutral tin atoms and lowly charged tin ions, SnI–SnV, is abundant in a wide variety of plasmas, ranging from laser-produced extreme-ultraviolet (EUV) light generating Sn plasma for nanolithography [1,2], divertor plasma when using tin-containing materials in future thermonuclear fusion reactors [3–5], and discharge plasma between tin whiskers causing short circuits [6] to astrophysical environments [7–15]. Spectroscopic investigations of these kinds of plasmas can help characterize plasma parameters [16–22] such as ion and electron densities and temperatures by study of the observed line strengths and their shapes. However, spectroscopic information on the relevant charge states Sn³⁺ and Sn⁴⁺, i.e., SnIV and SnV, is rather scarce, because of the poorly known electronic structure of these ions.

Sn³⁺, with its ground electronic configuration [Kr]$4d^{10}\,5s$, belongs to the Ag-like isoelectronic sequence. Remarkably, only the lowest eight singly excited $4d^{10}\,nl$, the doubly excited $4d^9\,5s^2$, and three $4d^9\,5s\,5p$ levels in Sn³⁺ are tabulated in the National Institute of Standards and Technology (NIST) Atomic Spectra Database (ASD) [23]. Level energies originate from unpublished work by Shenstone [24], while wavelengths are given in another compilation by the National Bureau of Standards [25]. The assessment of energy levels by Shenstone is based on extended and revised work by Lang and others [26–29]. Since the early compilation [24] of almost 60 years ago, the only extension of the electronic energy-level structure of SnIV stems from EUV spectroscopy by Ryabtsev and coworkers [30] in which they extend the $ns$ series from $n = 8$ up to $n = 10$ and add the $7d\,^2D$ term. A more extensive list of SnIV lines is given in an otherwise unpublished master's thesis [31]. In other works, beam-foil techniques have been used to determine lifetimes [32–34]. Besides the singly excited levels, some doubly excited energy levels belonging to the $4d^9\,5s\,5p$ configuration are identified in laser- and vacuum-spark-produced tin plasmas [30,35–39]. Theoretical level energies and transition probabilities [40,41] have been calculated for Ag-like ions. The narrow, inverted fine structure of the $4f\,^2F$ term in Ag-like Sn³⁺ has been

---

addressed in detail by theory [40–44]. In spite of all these efforts, knowledge of the electronic structure of SnIV is mostly limited to its lowest energy levels.

To obtain the electronic structure of $Sn^{3+}$, we have studied its line emission in the wavelength range of 200–800 nm. The optical lines belonging to SnIV are identified among the hundreds of optical lines stemming from a laser-produced droplet-based Sn plasma, by taking spectra as a function of the laser intensity. The method to single out transitions belonging to ions in a specific charge state relies on the strongly changing ratio between line intensity and background emission from the plasma as a function of the laser intensity.

In the following we first introduce and detail a convenient method to obtain charge-state-resolved optical spectra from a laser-produced plasma. Of the more than 350 lines observed in the visible spectral range, 53 are identified as stemming from $Sn^{3+}$. Of these, 33 lines are new determinations. Thereafter, line identification is discussed. On the basis of these line identifications an extended level diagram for $Sn^{3+}$ is constructed. The consistency of the highly excited levels is checked by quantum-defect scalings. In the final section, Fock-space coupled-cluster (FSCC) and configuration interaction many-body perturbation theory (CI+MBPT) calculations are employed to explain the anomalous behavior of the $5d\,^2D$ and $nf\,^2F$ terms.

## II. EXPERIMENTAL SETUP

An overview of the experimental setup is depicted in Fig. 1. A more detailed explanation is provided in Ref. [45]. The experimental laser-produced plasma source consists of a vacuum vessel (about $10^{-7}$ mb) equipped with a droplet generator from which a 10-kHz stream of liquid tin microdroplets is ejected. The droplets have a diameter of about 45 $\mu$m. A 10-Hz pulsed Nd:YAG laser, operating at its fundamental wavelength of 1064 nm, is used to irradiate the droplets in order to generate a plasma. The laser energy is varied
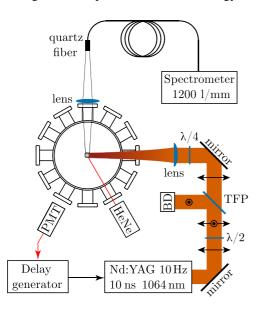


FIG. 1. Schematic top view of the main components of the laser-produced plasma source from which the spectroscopic data were taken. For details see Sec. II.

without changing the beam shape by using the combination of a half-wave plate ($\lambda/2$) and a thin-film polarizer (TFP), reflecting part of the light into a beamdump (BD). The laser beam is circularly polarized by a quarter-wave plate ($\lambda/4$); hereafter the beam is focused onto the droplet. This results in a Gaussian full-width-at-half-maximum (FWHM) beam size of 115 $\mu$m at the droplet position. The laser has a 10-ns FWHM pulse length. Light reflected by the droplet falling through a helium-neon (HeNe) laser sheet is detected by a photon-multiplier tube (PMT) used to trigger the laser.

The light emitted from the plasma is observed through a viewport perpendicular to the laser beam propagation and $30°$ above the horizontal plane. A biconvex lens images the plasma onto a quartz fiber that is used to guide the light to the spectrometer (Princeton Isoplane SCT 320). The entrance side of the fiber consists of 19 cores with a diameter of 200 $\mu$m in a hexagonal configuration, while at the exit side the cores are oriented in a linear configuration to efficiently guide light through the spectrometer slit. The spectrometer is laid out in a Czerny-Turner configuration with a focal length of 320 mm. The grating has 1200 lines per millimeter and is blazed at 500 nm, leading to a significantly reduced grating diffraction efficiency below 300 nm. A CCD camera (Princeton Pixis 2KBUV) optimized for the ultraviolet and visible regime recorded the diffracted light. By rotating the grating, thus changing the spectral detection range, the full spectral range from 200 to 800 nm is covered in steps of approximately 50 nm, overlapping by about 10 nm. From the shortest to the longest wavelength the linear dispersion decreases from 0.033 to 0.028 nm per pixel.

The wavelength axis is calibrated using neon-argon and mercury lamps. The FWHM line widths of the calibration lines are smaller than 0.1 nm. The total uncertainties of the mid positions of the $Sn^{3+}$ lines are better than 0.01 nm over all observed laser energies and wavelengths. The emitted light is space- and time-integrated by summing the intensity resulting from the various fiber cores and taking an integration time of 10 s, corresponding to 100 laser shots.

Measurements are performed with, and without, edge-pass filters to distinguish second-order lines from first-order ones. This enables filtering out the second-order lines appearing at wavelengths longer than 400 nm. Additionally, closely packed lines in the ultraviolet below 300 nm can be resolved in second order at a higher resolution. Weakly appearing lines at first order, due to the low grating response below 300 nm, are observed with a higher intensity at second order.

## III. CHARGE STATE IDENTIFICATION

We performed passive spectroscopy measurements on the laser-produced tin plasma for a series of laser energies ranging from 0.5 to 370 mJ. Figure 2 shows example measurements over a selected wavelength range for three laser energies, where it is shown that the number of lines increases with the laser energy. This is a signature of an increasing number of contributing charge states to the measured spectrum. A closer inspection indicates that indeed sets of lines appear with increasing laser energy that exhibit similar changes in intensity. As demonstrated below, each of these sets of lines
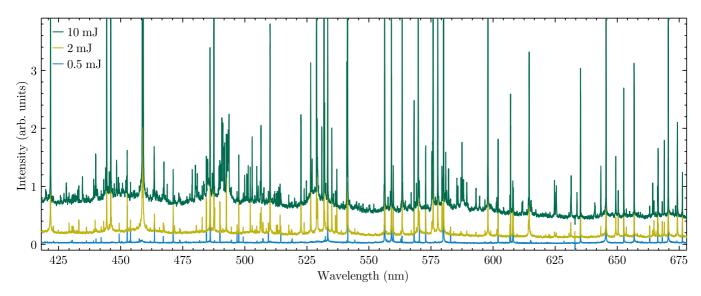
FIG. 2. Experimentally obtained Sn$^{q+}$ spectra for laser energies of 0.5 mJ (blue; lower), 2 mJ (yellow; middle), and 10 mJ (green; upper). The observable increase in the background level is due to increased continuum emission from the plasma at higher laser energies. Spectra shown are taken without spectral filters and, thus, include second-order contributions.

can be singled out by considering their intensities with respect to the continuum background, increasing strongly with the laser energy.

To illustrate the procedure we select a well-known line of each of the charge states SnI−SnV. These are the SnI $5p^2$ $^1S_0$–$5p\,6s\,^1P_1$ ($\lambda = 452.60$ nm [46]), SnII $5d\,^2D_{5/2}$–$4f\,^2F_{7/2}$ ($\lambda = 580.05$ nm [47]) (the transition from the $4f\,^2F_{5/2}$ at 579.85 nm is also visible), SnIII $6s\,^1S_0$–$6p\,^1P_1$ ($\lambda = 522.64$ nm [48]), SnIV $6s\,^2S_{1/2}$–$6p\,^2P_{1/2}$ ($\lambda = 421.73$ nm), and SnV $6s\,^3D_3$–$6p\,^3F_4$ ($\lambda = 315.6$ nm, based on level energies taken from Refs. [49] and [50]). The scaled intensity is defined as $I_\lambda/I_{bg} - 1$, with $I_\lambda$ the line intensity and $I_{bg}$ the (local value of the) continuum background level. For direct comparison, the scaled intensity of each individual line is normalized to its maximum value, as shown in Fig. 3. In Fig. 3, it is shown that for the lowest charge states SnI and SnII the normalized, scaled intensity maximizes for the lowest laser energy of 0.5 mJ, while for the highest observed charge state SnV a laser energy of 10 mJ is optimal. SnIV, the ion of interest here, maximizes at 2 mJ. This demonstrates that the contributions of higher charge states to the spectrum increase with increasing laser energy. Preliminary nanosecond time-resolved spectroscopic measurements revealed that spectral line emission is mostly observed in the late-time evolution of the plasma. Traces of line broadening are observed in the time-integrated spectra presented in this work, e.g., the SnIV line shape in the 2-mJ spectrum. Analysis of line-broadening mechanisms and the time evolution of these plasmas is left for future work, as they
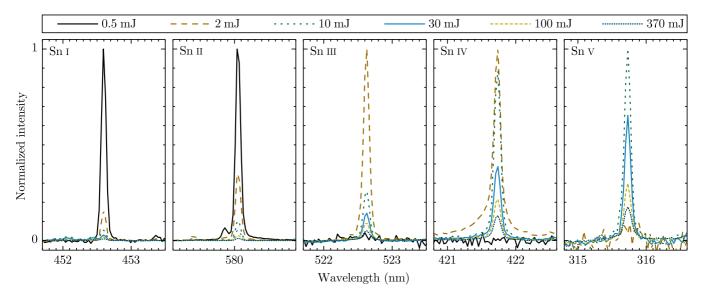


FIG. 3. Spectral intensity scaling as a function of the wavelength (vacuum; in nm) for varying laser energies. Here, the intensity is normalized to their (local) continuum background level, and unity is subsequently subtracted. The specific transitions shown are described in the text.

TABLE I. Vacuum wavelengths (in nm) of SnIV lines between levels previously known. Wavelengths determined in this work are compared with literature values taken from an otherwise unpublished master's thesis [31]. The upper and lower energy levels indicating the transition represent the $nl$ one-electron orbital outside the [Kr]$4d^{10}$ core configuration. The $5s^2$ indicates the doubly excited $4d^9 5s^2$ configuration. Wavelengths determined in this work are averaged centroid positions of Gaussian fits in spectra taken at different laser energies. The intensity $I$ represents the area under the curve of this line in the 30-mJ spectrum [in arbitrary (arb.) units]. $gA$ factors from the upper level result from analysis with the COWAN code.

| $\lambda$ (nm) | | $I$ | $gA$ | Lower | | Upper | |
|---|---|---|---|---|---|---|---|
| This work | Literature [31] | (arb. units) | ($10^8$ s$^{-1}$) | $nl$ | $J$ | $nl$ | $J$ |
| 208.23 | 208.224 | 25 | 130.2 | $4f$ | 7/2 | $5g$ | 9/2 |
| 208.49 | 208.485 | 20 | 100.4 | $4f$ | 5/2 | $5g$ | 7/2 |
| 222.14 | 222.156 | 28 | 53.8 | $5d$ | 3/2 | $4f$ | 5/2 |
| 222.66 | 222.680 | 1 | 3.4 | $5d$ | 5/2 | $4f$ | 5/2 |
| 222.96 | 222.980 | 34 | 68.5 | $5d$ | 5/2 | $4f$ | 7/2 |
| 243.75 | 243.757 | 35 | 6.6 | $5s^2$ | 5/2 | $4f$ | 7/2 |
| 251.47 | 251.466 | 22 | 6.0 | $6p$ | 1/2 | $7s$ | 5/2 |
| 266.05 | 266.054 | 48 | 10.1 | $6p$ | 3/2 | $7s$ | 1/2 |
| 270.68 | 270.667 | 154 | 27.5 | $6p$ | 1/2 | $6d$ | 3/2 |
| 284.91 | 284.922 | 351 | 42.2 | $6p$ | 3/2 | $6d$ | 5/2 |
| 287.64 | 287.633 | 38 | 4.6 | $6p$ | 3/2 | $6d$ | 3/2 |
| 287.96 | 287.961 | 32 | 1.5 | $5d$ | 3/2 | $6p$ | 3/2 |
| 288.85 | 288.840 | 219 | 11.2 | $5d$ | 5/2 | $6p$ | 3/2 |
| 307.26 | 307.247 | 251 | 6.0 | $5d$ | 3/2 | $6p$ | 1/2 |
| 324.71 | 324.700 | 166 | 1.6 | $5s^2$ | 5/2 | $6p$ | 3/2 |
| 386.23 | 386.232 | 1 063 | 9.2 | $6s$ | 1/2 | $6p$ | 3/2 |
| 402.08 | 402.071 | 289 | 4.5 | $4f$ | 7/2 | $6d$ | 5/2 |
| 403.03 | 403.076 | 30 | 0.2 | $4f$ | 5/2 | $6d$ | 5/2 |
| 408.52 | 408.520 | 219 | 3.0 | $4f$ | 5/2 | $6d$ | 3/2 |
| 421.73 | 421.735 | 677 | 3.5 | $6s$ | 1/2 | $6p$ | 1/2 |

do not influence our line identifications and are outside the scope of this paper.

Figure 4 quantifies the dependence of the scaled intensities for spectral lines belonging to tin ions in charge states 0, 1, 2, 3, and 4+ produced in the Sn laser-produced plasma. This energy dependence of each charge state enables us to make our assignments of unknown lines to specific charge states. In this way 53 lines are assigned to SnIV.

For our present experiments on tin ions we checked carefully the dependence of the intensities of all well-known tin lines on the laser energy. For each of the charge states the intensities of their well-known lines follow with some scatter the dependencies shown in Fig. 4. However, for adjacent charge states and weak lines with considerable scatter and that do not show up over the full laser energy range, there is a risk of ascribing such a weak line to the incorrect charge state. Solely based on the laser-energy dependence there were about five weaker lines that could be either SnIV or SnV. Even these lines could be attributed to either SnIV or SnV using the spectral identification procedure described in the next section (Sec. IV).

## IV. LINE IDENTIFICATION PROCEDURE

Of the 53 lines in the ultraviolet and optical spectral range attributed to SnIV, 20 are readily identified as transitions between energy levels known from the literature [24] and match well within mutual experimental uncertainties with the line positions given in Ref. [31]. These 20 lines are presented in Table I along with their connecting upper and lower energy levels.

Having identified 20 lines using known energy levels, we proceed with the identification of the other lines ascribed to SnIV. Unique identification of the observed lines requires an accuracy of the level energies of better than $10^{-3}$, which is challenging for atomic theories. Therefore, an iterative procedure is used to identify the unknown lines. We use the COWAN code to calculate the electronic structure and transitions and adjust its parameters to match perfectly the known lines in the spectrum. In this way, energy levels just above the known ones can be obtained with sufficient accuracy to identify the next set of lines. This procedure can be repeated to identify all lines. Furthermore, quantum defect theory [51] is used to check the consistency of level energies for each $l$ series.

### A. COWAN procedure

The COWAN code [52], one of the most widely applied electronic structure codes, is used to calculate the energies of yet unestablished SnIV levels. The COWAN code produces radial wave functions using a quasirelativistic Hartree-Fock method. The electrostatic single-configuration radial integrals $F_k$ and $G_k$ (Slater integrals), configuration interaction, Coulomb radial integrals, and spin-orbit parameters are calculated from the obtained wave functions. Subsequently, level energies and intermediate coupling eigenvectors are extracted.
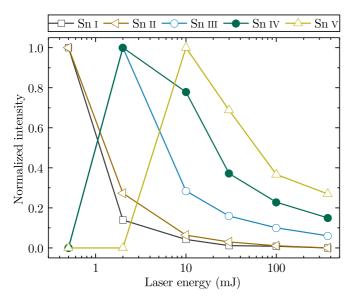
FIG. 4. Normalized scaled intensities of SnI–SnV lines as a function of the laser energy. The same lines as presented in Fig. 3 are used. Other SnI–SnV lines show a similar dependence on the laser energy.

Furthermore, values for the transition probabilities and wavelengths are obtained.

The values of the electrostatic integrals are scaled by a factor of between 0.7 and 0.85 as well as the scaling of spin-orbit parameters to optimally fit the thus far understood experimental spectrum. The outcome of this parameter scaling procedure yields a useful interpretation of the experimental spectrum. This enables predictions for lines between not yet experimentally established energy levels. These predictions include their relative strength expressed as the $gA$ factor: the Einstein coefficient $A$ multiplied with the statistical weight $g$ of the upper state. Due to the one-electron nature of the system, the number of allowed transitions between two terms is only three (or two if a $^2S$ term is involved). However, we might observe only two lines since transitions between equal angular momenta typically have a small $gA$ factor. Experimental lines that lie close to a predicted transition and have relative line strengths similar to those determined on the basis of the aforementioned $gA$ factors are thus assigned to a specific transition. This provides an enlarged set of levels that can be used to fine-tune the calculations in the next step.

### B. Quantum defect

The energy levels of quasi-one-electron systems approach a hydrogenlike level structure, especially for high principal and angular quantum numbers. For such systems the energy levels which are shifted towards slightly higher binding energies can be well described by introducing the so-called quantum defect $\delta_l$ as a correction to the Bohr formula. The position of the energy level $E_{nl}$ (relative to the ionization limit) is defined by [51]

$$E_{nl} = -R \frac{Z_c^2}{(n - \delta_l)^2}, \qquad (1)$$

with $Z_c$ the net charge state of the core ($Z_c = 4$ for Sn$^{3+}$) and $n$ the principal quantum number. $R$ relates to the Rydberg constant $R_\infty$ as $R = R_\infty (1 + m_e/M)^{-1}$, with $m_e$ and $M$ the electronic and nuclear mass, respectively. Following the review by Edlén [51], the quantum defect can be written as a Taylor expansion in $1/n^{*2}$, with $n^*$ being the apparent principal quantum number $n^* = n - \delta_l$, with quantum defect $\delta_l$,

$$\delta_l = a\left(\frac{1}{n^{*2}}\right) + b\left(\frac{1}{n^{*2}}\right)^2 + \cdots . \qquad (2)$$

The quantum defect becomes smaller with increasing angular momentum. For high-$n$ values the first term dominates and the minute change in $\delta_l$ as a function of $1/n^{*2}$ becomes linear. Additionally, it is well established that $a$ is positive for $l \leqslant l_{\text{core}}$, while $a$ is negative for $l > l_{\text{core}}$ [51]. For Sn$^{3+}$ with its $4d^{10}$ core, $l_{\text{core}} = 2$.

## V. RESULTS AND DISCUSSION

Using the iterative guidance from the COWAN code as described above, we assign the newly found lines. The new SnIV line assignments are summarized in Table II. The level energies of excited states are determined with respect to the $6s$, which is used as an anchor level considering that transitions to the $5s$ ground state are outside our detection region. The optimization of level energies is performed using Kramida's code LOPT [53], and the final results are presented in Table III.

The consistency of the energies of levels within a specific $l$ series is verified by determining the respective quantum defects. Quantum defects are calculated using Eq. (1) with the level energies found relative to the ionization limit. Therefore an accurate value of this limit is needed.

The ionization limit of 328 550 (300) cm$^{-1}$, tabulated in the NIST ASD [23], is based on the determination of the series limit of the $ns$ levels ($n = 5$–7). Ryabtsev et al. [30] extended this $ns$ series with $8s$, $9s$, and $10s$. Using the extended $ns$ series they were able to refine the ionization limit to 328 910 (5) cm$^{-1}$. The ionization limit can be further improved by taking additional levels into account. Configurations which are prone to shifting of the level energies by configuration interaction effects ($np$, $nd$, and $nf$, further described in Sec. V C) are, however, unsuitable for determining the series limit. Therefore we only use the $ng$, $nh$, and $ni$ configurations to refine the ionization limit. The results from analysis with the POLAR code [54] is 328 908.4 cm$^{-1}$, with a statistical error of 0.3 cm$^{-1}$. Combining this in quadrature with the uncertainty of the $6s$ anchor level, we arrive at a total uncertainty of 2.1 cm$^{-1}$. Figure 5 presents the quantum defects of the SnIV levels as a function of $1/n^{*2}$. Overall, a smooth dependence is found for all angular quantum numbers from $l = 0$ ($s$) up to $l = 6$ ($i$), underpinning the consistency of our identifications.

For the discussion of details of the line assignments and energy levels we consider separately levels for which the valence electron does or does not penetrate the electronic core, i.e., levels with $l \leqslant l_{\text{core}}$ and $l > l_{\text{core}}$, respectively. For Sn$^{3+}$ with its $4d^{10}$ core, $l_{\text{core}} = 2$. Anomalous effects on the fine-structure splitting of the $5d$ and $nf$ configurations are

TABLE II. Assignments and vacuum wavelengths (in nm) of UV and visible transitions of SnIV identified in this work. The upper and lower energy levels indicating the transition represent the $nl$ one-electron orbital outside the $[Kr]4d^{10}$ core configuration. Wavelengths determined in this work are averaged centroid positions of Gaussian fits in spectra taken at different laser energies. The intensity $I$ represents the area under the curve of this line in the 30-mJ spectrum [in arbitrary (arb.) units]. $gA$ factors from the upper level result from analysis with the COWAN code. The fine structure for several high-$l$ states could not be resolved experimentally, therefore no individual angular momenta are listed and the reported $gA$ is the summed value of the three possible transitions.

| $\lambda$ | $I$ | $gA$ | Lower | | Upper | |
|---|---|---|---|---|---|---|
| (nm) | (arb. units) | $(10^8 \text{ s}^{-1})$ | $nl$ | $J$ | $nl$ | $J$ |
| 202.08 | 1 | 10.5 | 5f | 7/2 | 8g | 9/2 |
| 203.36 | 2 | 8.6 | 5f | 5/2 | 8g | 7/2 |
| 231.72 | 2 | 14.4 | 5g | | 8h | |
| 242.55 | 3 | 0.3 | 6d | 3/2 | 6f | 5/2 |
| 245.15 | 1 | 0.5 | 6d | 5/2 | 6f | 7/2 |
| 273.75 | 3 | 2.2 | 7p | 1/2 | 8d | 3/2 |
| 279.91 | 8 | 3.8 | 7p | 3/2 | 8d | 5/2 |
| 287.82 | 48 | 30.4 | 5g | | 7h | |
| 357.01 | 204 | 24.6 | 5f | 7/2 | 6g | 9/2 |
| 360.99 | 233 | 20.2 | 5f | 5/2 | 6g | 7/2 |
| 393.41 | 27 | 5.7 | 6f | 7/2 | 8g | 9/2 |
| 395.08 | 35 | 4.4 | 6f | 5/2 | 8g | 7/2 |
| 459.04 | 2 518 | 93.7 | 5g | | 6h | |
| 463.49 | 202 | 15.1 | 6g | | 8h | |
| 467.41 | 107 | 14.7 | 6h | | 8i | |
| 504.82 | 90 | 2.0 | 7p | 1/2 | 8s | 1/2 |
| 529.12 | 40 | 3.5 | 7p | 3/2 | 8s | 1/2 |
| 541.12 | 366 | 7.9 | 7p | 1/2 | 7d | 3/2 |
| 563.38 | 662 | 12.4 | 7p | 3/2 | 7d | 5/2 |
| 563.60 | 60 | 0.7 | 5g | 7/2 | 6f | 5/2 |
| 567.00 | 42 | 0.9 | 5g | 9/2 | 6f | 7/2 |
| 569.13 | 68 | 1.3 | 7p | 3/2 | 7d | 3/2 |
| 575.85 | 881 | 10.0 | 6d | 3/2 | 5f | 5/2 |
| 589.40 | 71 | 6.9 | 6f | 7/2 | 7g | 9/2 |
| 593.13 | 63 | 5.3 | 6f | 5/2 | 7g | 7/2 |
| 597.93 | 940 | 12.5 | 6d | 5/2 | 5f | 7/2 |
| 643.43 | 154 | 3.3 | 5f | 7/2 | 7d | 5/2 |
| 664.32 | 103 | 2.3 | 5f | 5/2 | 7d | 3/2 |
| 673.51 | 36 | 0.5 | 6d | 3/2 | 7p | 3/2 |
| 688.89 | 212 | 3.8 | 6d | 5/2 | 7p | 3/2 |
| 717.44 | 98 | 1.8 | 6d | 3/2 | 7p | 1/2 |
| 759.65 | 316 | 49.6 | 6g | | 7h | |
| 769.75 | 380 | 49.6 | 6h | | 7i | |

discussed and explained separately. Finally, Fig. 6 depicts the extended level diagram of SnIV as a concise summary of our results.

### A. $l \leqslant l_{\text{core}}$ configurations

The 5s, 6s, and 7s levels are included in Moore's tables [24]. The excitation energies of the 8s, 9s, and, 10s levels were determined in EUV spectroscopy experiments by Ryabtsev *et al.* [30] in which transitions to the $5p\,^2P_{1/2,3/2}$ terms were measured. The $5p\,^2P_{1/2,3/2}$ terms can be populated from the $nd$ series; this $nd$ series is known up to $n = 7$. The highest known $np$ configuration so far was $6p$. All transitions

in the optical spectral range (Table II) between both $ns$ and $nd$ and $6p$ agree with the literature excitation energies of the respective levels.

The $7p\,^2P_{1/2,3/2}$ levels are found by considering all possible transitions from the $7d\,^2D_{3/2,5/2}$ and $8s\,^2S_{1/2}$ to the $7p\,^2P_{1/2,3/2}$ levels. These levels can decay via emission in the visible to $6d\,^2D_{3/2,5/2}$. The excitation energies of the $7p$ configuration are established using seven transitions to three surrounding energy terms, providing a reliable assessment of the $7p\,^2P_{1/2,3/2}$ level energies. For the $7d\,^2D_{5/2}$ good agreement with Ref. [30] is found, while for the $7d\,^2D_{3/2}$ level a difference of about 30 cm$^{-1}$ is observed. The $8d$ is successively determined using two transitions to the $7p$, where

TABLE III. Energy levels of Sn$^{3+}$, with its ground state [Kr]$4d^{10}5s$. The experimental values obtained in this work are presented, next to the known values from the literature given in Refs. [24] and [30]. Experimental level energies of excited states are calculated with respect to the $6s$ anchor level and are the results of analysis with the LOPT code. The statistical uncertainty is presented in parentheses. The "Total" column lists the sums of FSCC calculations including Breit interaction and QED effects. As a comparison to theoretical values, relativistic many-body perturbation theory (RMBPT) calculations obtained from Ref. [40] are listed, while other known fine-structure splittings are reported in Table IV. The fine-structure splittings of several high-$nl$ levels are smaller than 0.5 cm$^{-1}$ and not resolved experimentally. In these cases, the value of the angular momentum is omitted. The ionization potential (IP) is presented at the bottom.

| | | $E_{\text{experiment}}$ (cm$^{-1}$) | | $E_{\text{theory}}$ (cm$^{-1}$) | | | | |
|---|---|---|---|---|---|---|---|---|
| $nl$ | $J$ | This work | Literature | FSCC | $\Delta E_{\text{Breit}}$ | $\Delta E_{\text{QED}}$ | Total | RMBPT [40] |
| $5p$ | 1/2 | | 69 563.9 [24] | 69 850 | 62 | −171 | 69 741 | 69 265 |
| | 3/2 | | 76 072.3 [24] | 76 447 | −26 | −165 | 76 256 | 75 736 |
| $5d$ | 3/2 | 165 304(1) | 165 304.7 [24] | 165 974 | −123 | −205 | 165 646 | 164 538 |
| | 5/2 | 165 409(1) | 165 410.8 [24] | 166 731 | −145 | −204 | 166 382 | 165 283 |
| $4d^9 5s^2$ | 5/2 | 169 233.6(8) | 169 233.6 [24] | | | | | |
| | 3/2 | | 177 889.0 [24] | | | | | |
| $6s$ | 1/2 | 174 138.8(4) | 174 138.8 [24] | 174 478 | −99 | −143 | 174 236 | |
| $6p$ | 1/2 | 197 850.6(6) | 197 850.9 [24] | 198 292 | −74 | −193 | 198 025 | |
| | 3/2 | 200 030.1(4) | 200 030.8 [24] | 200 512 | −103 | −193 | 200 216 | |
| $4f$ | 7/2 | 210 258.2(6) | 210 257.7 [24] | 210 912 | −158 | −200 | 210 554 | 209 418 |
| | 5/2 | 210 317.9(7) | 210 318.2 [24] | 210 983 | −156 | −200 | 210 627 | 209 494 |
| $6d$ | 3/2 | 234 797.0(1) | 234 795.7 [24] | 235 509 | −134 | −203 | 235 171 | |
| | 5/2 | 235 128.7(2) | 235 127.7 [24] | 235 842 | −144 | −201 | 235 497 | |
| $7s$ | 1/2 | 237 617(1) | 237 615.7 [24] | 238 219 | −123 | −175 | 237 920 | |
| $7p$ | 1/2 | 248 735.4(2) | | 249 402 | −110 | −197 | 249 094 | |
| | 3/2 | 249 644.8(1) | | 250 454 | −124 | −97 | 250 233 | |
| $5f$ | 7/2 | 251 853.0(2) | | 252 984 | −157 | −201 | 252 626 | 250 981 |
| | 5/2 | 252 162.6(2) | | 253 023 | −155 | −202 | 252 666 | 251 025 |
| $5g$ | 7/2 | 258 283.2(3) | 258 282.3 [24] | 258 782 | −143 | −201 | 258 439 | 256 868 |
| | 9/2 | 258 283.2(3) | 258 282.7 [24] | 258 782 | −143 | −201 | 258 439 | 256 872 |
| $7d$ | 3/2 | 267 215.5(2) | 267 247.6 [30] | 267 815 | −138 | −202 | 267 475 | |
| | 5/2 | 267 394.7(2) | 267 395.7 [30] | 267 993 | −143 | −203 | 267 647 | |
| $8s$ | 1/2 | 268 544.3(3) | 268 544 [30] | 269 193 | −132 | −166 | 268 895 | |
| $6f$ | 7/2 | 275 919.8(3) | | 276 430 | −153 | −201 | 276 076 | |
| | 5/2 | 276 026.2(3) | | 276 450 | −152 | −201 | 276 097 | |
| $6g$ | 9/2 | 279 863.6(2) | | 280 580 | −143 | −202 | 280 235 | |
| | 7/2 | 279 863.6(2) | | 280 581 | −143 | −201 | 280 237 | |
| $6h$ | | 280 067.8(7) | | | | | | |
| $8d$ | 3/2 | 285 265(1) | | 285 834 | −140 | −197 | 285 497 | |
| | 5/2 | 285 370(1) | | 285 937 | −143 | −197 | 285 597 | |
| $9s$ | 1/2 | | 286 013 [30] | | | | | |
| $7g$ | | 292 886.0(3) | | | | | | |
| $7h$ | | 293 027.6(3) | | | | | | |
| $7i$ | | 293 059.0(2) | | | | | | |
| $10s$ | 1/2 | | 296 844 [30] | | | | | |
| $8g$ | | 301 338.2(6) | | | | | | |
| $8h$ | | 301 439.2(7) | | | | | | |
| $8i$ | | 301 462.3(7) | | | | | | |
| IP | | 328 908.4(3) | 328 550 [24] | 329 343 | −143 | −201 | 328 999 | 327 453 |
| | | | 328 910 [30] | | | | | |

the transition between equal angular momenta is likely too weak to be observed in our spectra.

The quantum defects for $l \leqslant l_{\text{core}}$ are shown in Fig. 5, calculated using the refined ionization limit. All data points exhibit a linear behavior, with only the lowest $5l$ configurations slightly deviating, reflecting a signature of the small quadratic term in Eq. (2). The most remarkable observation is the almost-equal quantum defects of the $5d\ ^2D_{3/2,5/2}$ levels, indicative of an anomalously small fine-structure interval

of the $5d\ ^2D$ term. This anomaly is further discussed in Sec. V C.

## B. $l > l_{\text{core}}$ configurations

Of the high-$l$ configurations, i.e., $nf$, $ng$, $nh$, and $ni$, only the level energies of the $4f\ ^2F$ and $5g\ ^2G$ terms were known thus far. Our measurements confirm the small inverted fine-structure splitting of approximately 60 cm$^{-1}$ of the $4f\ ^2F$ term

TABLE IV. Comparison of fine-structure splittings in $np$, $nd$, and $nf$ configurations of SnIV. Experimental values stem either from a direct comparison of $\Delta J = 0$ and $\Delta J = -1$ transitions or indirectly from the optimized level structure. The latter values are followed by an asterisk. The upper part of the table lists results published in this work; the lower part, results obtained from Refs. [24] and [40–44].

| | Fine-structure splitting (cm$^{-1}$) | | | | | | | | | |
|---|---|---|---|---|---|---|---|---|---|---|
| | $5p$ | $6p$ | $7p$ | $5d$ | $6d$ | $7d$ | $8d$ | $4f$ | $5f$ | $6f$ |
| Experiment | | 2 179.5 | 909.1 | 107.0 | 331.1 | 179.3 | 105.4* | −60.4 | −309.6* | −106.4* |
| COWAN | 6 417 | 2 237 | 911 | 170 | 240 | 130 | 79 | 34 | −228 | −73 |
| FSCC | 6 515 | 2 191 | 1 139 | 736 | 326 | 172 | 100 | −73 | −40 | −21 |
| CI+MBPT | | | | 162 | | | | | −620 | |
| Experiment [24] | 6 508.4 | 2 179.9 | | 106.1 | 332.0 | | | −60.5 | | |
| RMBPT [40] | 6 471 | | | 745 | | | | −76 | −44 | |
| RPTMP[a] [41] | | | | | | | | −60 | −22 | |
| MCDHF [42] | | | | | | | | −71 | | |
| FCV [43] | | | | | | | | −85 | | |
| RHF[a] [44] | 5 960 | | | 641 | | | | −108 | −72 | |

[a]Fine-structure splittings deduced from transition wavelengths.

and of about 0.5 cm$^{-1}$ of the $5g\ ^2G$ by direct comparison of the $\Delta J = 0$ and $\Delta J = -1$ transitions. The $4f\ ^2F$ and $5g\ ^2G$ terms form the main basis on which the excitation energies of the high-$l$ configurations are determined. Fine-structure splittings of the $ng\ ^2G$ ($n \geqslant 6$), $nh\ ^2H$, and $ni\ ^2I$ terms are too small to be determined, implying that their fine-structure splitting is less than 0.5 cm$^{-1}$. The fine-structure splittings of the $nf$ terms are presented in Table IV and discussed in detail in Sec. V C.

The first level of the $nh$ series, $6h$, is found by assigning the strong transition from this level to $5g$. The $6h$ is the lower level of the transitions determining the $7i$ and $8i$. The $7h$ and $8h$ are found by transitions to the $6g$, which is based on the transition to the $5f\ ^2F$. The $ng\ ^2G$ ($n \geqslant 7$) are determined from their transitions to the $5f\ ^2F$ and $6f\ ^2F$ terms. The $5f$ and $6f$ terms are defined by transitions to their lower-lying $nd\ ^2D$ counterparts.

The relative values of the quantum defects for the $ng$, $nh$, and $ni$ series are in good agreement with the $nl$ scaling laws for $l > l_{\text{core}}$ as presented by Edlén [51]. The quantum defects for the $nf$ series are about a factor of 3 to 4 larger than expected from these scaling laws. In addition, relatively large fine-structure splittings are observed for the $5f\ ^2F$ and $6f\ ^2F$ terms. Both effects may be a signature of an enhanced interaction with core-electron configurations.

### C. Anomalous fine-structure effects in the $5d\ ^2D$ and $nf\ ^2F$ terms

Table IV summarizes experimental and theoretical fine-structure intervals in SnIV. We have performed Fock-space coupled-cluster and configuration interaction many-body perturbation theory in order to address the aforementioned anomalous values of the fine-structure intervals in the $5d\ ^2D$ and $nf\ ^2F$ terms.

FSCC calculations of the transition energies were performed within the framework of the projected Dirac-Coulomb-Breit (DCB) Hamiltonian [55],

$$H_{\text{DCB}} = \sum_i h_D(i) + \sum_{i<j} (1/r_{ij} + B_{ij}). \quad (3)$$

Here, $h_D$ is the one-electron Dirac Hamiltonian,

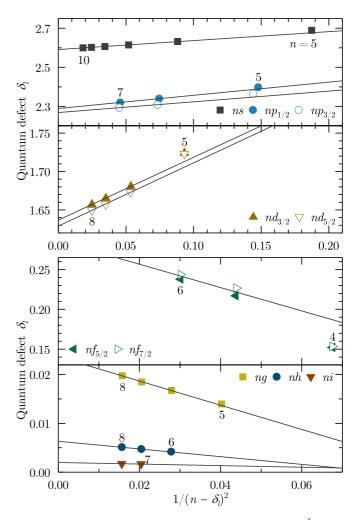$$h_D(i) = c\boldsymbol{\alpha}_i \cdot \mathbf{p}_i + c^2\beta_i + V_{\text{nuc}}(i), \quad (4)$$



FIG. 5. Quantum defect values as a function of the $1/n^{*2}$ of the SnIV energy levels, for $l \leqslant l_{\text{core}}$ (top) and $l > l_{\text{core}}$ (bottom). Quantum defects are calculated using Eq. (1) and the refined ionization limit of 328 908.4 cm$^{-1}$. Black lines are linear fits of the data points where the lowest level is excluded (except for the $ni$ configuration).
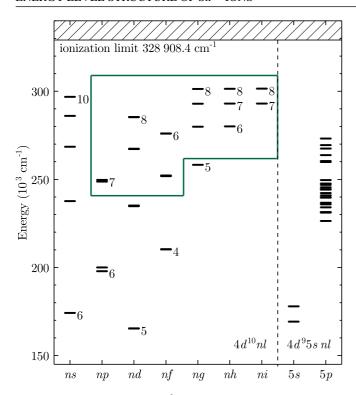
FIG. 6. Level diagram of Sn³⁺, drawn from 150 000 cm⁻¹ to the ionization limit at 328 908.4 cm⁻¹. The ground state 5s, the 5p ²P term, and multiply excited configurations lying near the ionization limit are omitted, as transitions to these levels occur outside the detection range of this study. The levels determined in this study are shown in the boxed area. Other levels are based on Refs. [24] and [30].

where $\boldsymbol{\alpha}$ and $\beta$ are the four-dimensional Dirac matrices. The nuclear potential $V_{\text{nuc}}(i)$ takes into account the finite size of the nucleus, modeled by a uniformly charged sphere [56]. The two-electron term includes the nonrelativistic electron repulsion and the frequency-independent Breit operator,

$$B_{ij} = -\frac{1}{2r_{ij}}\big[\boldsymbol{\alpha}_i \cdot \boldsymbol{\alpha}_j + (\boldsymbol{\alpha}_i \cdot \mathbf{r}_{ij})(\boldsymbol{\alpha}_j \cdot \mathbf{r}_{ij})/r_{ij}^2\big], \quad (5)$$

and is correct to second order in the fine-structure constant $\alpha$.

The calculations of the transition energies of Sn³⁺ start from the closed-shell reference [Kr]4d¹⁰ configuration of Sn⁴⁺. After the first stage of the calculation, consisting of solving the relativistic Hartree-Fock equations and correlating the closed-shell reference state, a single electron was added to reach the desired Sn³⁺ state. A large model space was used in this calculation, comprising 10 s, 8 p, 6 d, 6 f, 4 g, 3 h, and 2 i orbitals in order to obtain a large number of excitation energies and to reach optimal accuracy. The intermediate Hamiltonian method was employed to facilitate convergence [57].

The uncontracted universal basis set [58] was used, consisting of even-tempered Gaussian-type orbitals, with exponents given by

$$\xi_n = \gamma \delta^{(n-1)}, \quad \gamma = 106\,111\,395.371\,615,$$
$$\delta = 0.486\,752\,256\,286. \quad (6)$$

The basis set was composed of 37 s, 31 p, 26 d, 21 f, 16 g, 11 h, and 6 i functions; the convergence of the obtained transition energies with respect to the size of the basis set was verified. All the electrons were correlated.

FSCC calculations were performed using the Tel-Aviv Relativistic Atomic FSCC code (TRAFS-3C) [59]. To account for the QED corrections to the transition energies we applied the model Lamb shift operator of Shabaev and coworkers [60] to the atomic no-virtual-pair, many-body DCB Hamiltonian as implemented in the QEDMOD program. Our implementation of the model Lamb shift operator formalism into the Tel Aviv atomic computational package allows us to obtain the vacuum polarization and self-energy contributions beyond the usual mean-field level, namely, at the DCB-FSCCSD level.

The FSCC results are compared to the experimental level energies and several results from previous theoretical work in Table III and are overall in good agreement. Typical differences from experiment are about 100 to 300 cm⁻¹, which is on the 10⁻³ level of the calculated excitation energies. Concerning the measured anomalous fine-structure intervals of the 5d ²D and 5f ²F and 6f ²F terms, listed in Table IV, the apparent narrowing of the fine-structure interval of the 5d ²D term and the widening of the 5f ²F and 6f ²F term intervals are not reproduced by the FSCC calculations. The FSCC intervals are similar to those presented in earlier theoretical investigations [40–44].

For the 5d ²D term the fine-structure interval is measured at 107 cm⁻¹, while all theoretical results are higher by a factor of approximately 7 (see Table IV). Upon inspecting the level diagram (Fig. 6) one notes that the 5d ²D term might suffer from configuration interaction of the doubly excited 4d⁹ 5s² levels.

To quantify the strength of the configuration interaction we employ CI+MBPT calculations using the AMBiT code. Details of the AMBiT code can be found in Refs. [61–64]. To begin our discussion of the AMBiT treatment of the problem, first consider the 5d ²D₅/₂ and 4d⁹ 5s² ²D₅/₂ levels as a two-level system. In the absence of interaction between them, they have theoretical energies $\epsilon_1$ and $\epsilon_2$, respectively. $\epsilon_1$ is, to a good approximation, the FSCC value of the 5d ²D₅/₂ level, since in that calculation the one-hole two-particle 4d⁹ 5s² ²D₅/₂ level is not explicitly included. If we now add an interaction $V$, then the states mix and the levels repel each other.

The Hamiltonian of this two-level system is

$$H = \begin{pmatrix} \epsilon_1 & V \\ V & \epsilon_2 \end{pmatrix}.$$

Writing $\Delta\epsilon = \epsilon_2 - \epsilon_1 > 0$, the 5d ²D₅/₂ level shifts down by an amount

$$\delta = \frac{\Delta E - \Delta\epsilon}{2} = \frac{\Delta\epsilon}{2}\left(\sqrt{1 + \frac{4V^2}{\Delta\epsilon^2}} - 1\right) = b^2 \Delta E, \quad (7)$$

where $\Delta E = E_2 - E_1$ is the difference between the eigenvalues of $H$ and $b$ is the smaller component of the normalized eigenvector $(a, b)^{\mathsf{T}}$.

Using AMBiT, we calculate theoretical values for the parameters $\Delta E_{\text{th}}$ and $b$, from which we can obtain the interaction $V = -ab\Delta E_{\text{th}}$. However, the values of $\Delta E_{\text{th}}$ and $b$ are sensitive to details of the calculations. In particular, it

is challenging to match theoretical with experimental level energies at a good level of accuracy. On the other hand, the values of $V$ that we obtain are highly stable since they are not sensitive to the separation. If we use the experimental separation $\Delta E_{\exp} = 3\,823$ cm$^{-1}$ and $|V| = 1\,523$ cm$^{-1}$ from AMBiT, we find the energy shift of the $5d\,^2D_{5/2}$ level due to interaction with the hole state,

$$\delta = \frac{\Delta E_{\exp}}{2}\left(1 - \sqrt{1 - \frac{4V^2}{\Delta E_{\exp}^2}}\right), \qquad (8)$$

yielding $-755$ cm$^{-1}$. The $5d\,^2D_{3/2}$ level also shifts down due to interaction with the $4d^9\,5s^2\,^2D_{3/2}$ hole level. However, the energy difference is three times larger, and since $b \sim 1/\Delta E$, the energy shift is smaller by approximately a factor of 3. We calculate $|V| = 1498$ cm$^{-1}$ for this pair of levels, so Eq. (8) gives a level shift of $-181$ cm$^{-1}$. The change in the $5d$ fine-structure splitting is therefore $-574$ cm$^{-1}$, which is close to the difference between experiment and the FSCC calculation of $-629$ cm$^{-1}$.

In support of the role of the configuration interaction in the $5d\,^2D$ fine structure, FSCC calculations were performed for isoelectronic In$^{2+}$ ions, in which there is a much larger energy difference between the $5d\,^2D$ term and the doubly excited $4d^9\,5s^2\,^2D_{5/2}$ level [24]. Thus a better agreement with FSCC calculations is expected. In comparison to Sn$^{3+}$, for In$^{2+}$ the difference between experiment [24] and the FSCC indeed reduces strongly, from a factor of 7 to only 30% (298 versus 398 cm$^{-1}$).

Before discussing the impact of configuration interaction on the fine structure of the $5f\,^2F$ and $6f\,^2F$ terms we note that the $4f\,^2F$ exhibits an inverted fine structure, with the $J = 7/2$ level being more strongly bound than the $J = 5/2$ level by approximately 60 cm$^{-1}$. The occurrence of this inversion of the fine structure and the actual value of the fine-structure interval results from an intricate balance between relativistic, spin-orbit and core polarization effects and has been the subject of a variety of theoretical approaches calculating the $4f\,^2F$ fine structure along the isoelectronic sequence of Ag-like ions [40–44].

We confirm the fine structure of the $4f\,^2F$ term by measuring the wavelengths of the transitions from the $5g\,^2G$ levels and the transitions to the $5d\,^2D$ levels. Weaker transitions from the $6d\,^2D$ term to the doubly excited $4d^9\,5s^2\,^2D_{5/2}$ level are observed in addition. A comparison of the fine-structure splitting of the observed $nf\,^2F$ levels with theoretical calculations is given in Table IV. Both measurements and theoretical calculations agree on an inverted fine-structure splitting for these $nf\,^2F$ terms. However, the magnitudes of the fine-structure splitting of the $5f$ and $6f$ terms are much smaller than our experimental ones.

In similar fashion to the $5d\,^2D$ levels, the $5f\,^2F$ fine-structure splitting is strongly affected by interaction with hole states. However, the $5f\,^2F$ case is more complicated because the $4d^9\,5s\,5p$ configuration has seven configuration state functions (CSFs) with $J = 5/2$ and four CSFs with $J = 7/2$. The CSFs tend to be strongly mixed with each other and, also, have small contributions of CSFs belonging to other configurations. Therefore, rather than treat the system as a few-level system, we use the approach of perturbation theory.

TABLE V. Sn IV $4d^9\,5s\,5p$ level energies as candidates for possible configuration interaction with the $nf$ levels. Level energies are obtained from COWAN code calculations published in Ref. [30]. Matrix elements $|V_{i,5f}|$ are calculated using the AMBiT code. The resulting shift of the $5f$ level by configuration interaction by the level is given by $\delta_{5f}$. The $J = 5/2$ levels interact with the $5f\,^2F_{5/2}$; similarly, the $J = 7/2$ levels, with the $5f\,^2F_{7/2}$.

| $E_i$ (cm$^{-1}$) [30] | $J$ | $|V_{i,5f}|$ | $\delta_{5f}$ |
|---|---|---|---|
| 226 363 | 5/2 | 3 | 0 |
| 231 318 | 5/2 | 484 | 11 |
| 239 582 | 5/2 | 765 | 47 |
| 242 203 | 5/2 | 622 | 39 |
| 249 541 | 5/2 | 41 | 1 |
| 263 718 | 5/2 | 111 | $-1$ |
| 269 440 | 5/2 | 1341 | $-104$ |
| 231 090 | 7/2 | 72 | 0 |
| 239 920 | 7/2 | 417 | 15 |
| 246 851 | 7/2 | 601 | 72 |
| 260 398 | 7/2 | 2404 | $-676$ |

Using AMBiT we obtain energies for the $4d^9\,5s\,5p$ levels as well as a mixing coefficient. At first order in perturbation theory, the coefficient of $\psi_{5f}$ in level $\psi_i$ is simply

$$b_{5f} = \frac{V_{i,5f}}{E_i - E_{5f}}.$$

From our AMBiT values of $b_{5f}$ and $E_i$, we extract values for the matrix element $V_{i,5f}$. Again, these are relatively stable for different calculations, even though the energies and $b$ coefficients can change dramatically.

The corresponding energy shift of the $5f$ level is $\delta_{5f} = V_{i,5f}^2/\Delta E_{\exp}$. Unfortunately we do not have precise experimental determinations of most of the interaction $4d^9\,5s\,5p$ levels. Instead we use the results of COWAN calculations [30] to obtain an approximation to the level shifts. The results are presented in Table V.

We see that while each of the $5f$ levels is shifted by interactions with the hole levels, the change in the fine-structure splitting is dominated by the interaction of the $5f\,^2F_{7/2}$ level with a hole state at 260 398 cm$^{-1}$. The final expected shift is 580 cm$^{-1}$, overestimating the actual difference between experimental fine-structure and FSCC calculations of 270 cm$^{-1}$. Nevertheless, given the uncertainties in our estimation of $V$ and the location of the doubly excited levels, we arrive at a plausible explanation for the observed anomaly.

A similar explanation can be given for the observed difference in fine-structure splitting for the $6f\,^2F$ term, interacting with the high-lying levels in the same series of hole states. Because the energy differences between these levels are larger, this effect may reasonably be expected to be smaller than for the $5f\,^2F$ levels. Likewise, the $7p\,^2P$ is expected to interact with several doubly-excited levels.

We also performed COWAN calculations to investigate the terms described above. The number of fitted parameters in this case is reduced by tying the Hartree-Fock ratios to the spin-orbit parameters for the $np$, $nd$, and $nf$ levels. The $4d^9\,5s\,5p$ levels are taken from Ref. [30] (included in Table V). The

two $4d^9\,5s^2\,^2D$ levels were calculated with two adjustable parameters. All interaction parameters were fixed at 0.8 of their Hartree-Fock values. The number of levels determined was insufficient to more accurately fit the parameters. Results of the calculation are listed in Table IV and show good agreement with the experimental results, although the inversion of the $4f\,^2F$ level is not reproduced. The agreement for all other $nf$ and the $np$ and $nd$ levels underlines the significant role of configuration interaction in a quasi-one-electron system like Sn$^{3+}$.

## VI. CONCLUSION

Optical techniques are useful diagnostics in plasma sources of EUV light in nanolithography. We present the ultraviolet and optical spectra of a laser-produced tin plasma. The lines belonging to Sn$^{3+}$ are identified using a convenient masking technique. The 33 newly found lines are used to determine 13 new configurations with iterative guidance from COWAN code calculations. The level energies are verified using a quantum-defect scaling procedure, leading to the refinement of the ionization limit to $328\,908.4$ cm$^{-1}$, with an uncertainty of $2.1$ cm$^{-1}$. FSCC calculations are generally in good agreement with the present measurements. The anomalous behavior of the $5d\,^2D$ and $nf\,^2D$ terms is shown to arise from configuration interaction with doubly excited levels by joining the strengths of the FSCC, COWAN, and CI+MBPT approaches.

[1] V. Y. Banine, K. N. Koshelev, and G. H. P. M. Swinkels, J. Phys. D **44**, 253001 (2011).

[2] W. Svendsen and G. O'Sullivan, Phys. Rev. A **50**, 3710 (1994).

[3] J. W. Coenen, G. De Temmerman, G. Federici, V. Philipps, G. Sergienko, G. Strohmayer, A. Terra, B. Unterberg, T. Wegener, and D. C. M. van den Bekerom, Phys. Scr. **T159**, 014037 (2014).

[4] G. G. van Eden, T. W. Morgan, D. U. B. Aussems, M. A. van den Berg, K. Bystrov, and M. C. M. van de Sanden, Phys. Rev. Lett. **116**, 135002 (2016).

[5] G. G. Eden, V. Kvon, M. C. M. van de Sanden, and T. W. Morgan, Nat. Commun. **8**, 192 (2017).

[6] M. S. Mason and G. Eng, J. Vac. Sci. Technol. A **25**, 1562 (2007).

[7] L. M. Hobbs, D. E. Welty, D. C. Morton, L. Spitzer, and D. G. York, Astrophys. J. **411**, 750 (1993).

[8] C. R. Proffitt, C. J. Sansonetti, and J. Reader, Astrophys. J. **557**, 320 (2001).

[9] P. Chayer, S. Vennes, J. Dupuis, and J. W. Kruk, Astrophys. J. Lett. **630**, L169 (2005).

[10] S. J. Adelman, W. P. Bidelman, and D. M. Pyper, Astrophys. J. Suppl. Ser. **40**, 371 (1979).

[11] B. D. Savage and K. R. Sembach, Annu. Rev. Astron. Astrophys. **34**, 279 (1996).

[12] U. J. Sofia, D. M. Meyer, and J. A. Cardelli, Astrophys. J. Lett. **522**, L137 (1999).

[13] I. de Andrés-García, A. Alonso-Medina, and C. Colón, Mon. Not. R. Astron. Soc. **455**, 1145 (2016).

[14] M. S. Dimitrijević, Z. Simić, R. Stamm, J. Rosato, N. Milovanović, and C. Yubero, Atoms **6**, 10 (2018).

[15] S. Biswas, A. Das, A. Bhowmik, and S. Majumder, Mon. Not. R. Astron. Soc. **477**, 5605 (2018).

[16] A. Roy, S. S. Harilal, S. M. Hassan, A. Endo, T. Mocek, and A. Hassanein, Laser Part. Beams **33**, 175 (2015).

[17] R. W. Coons, S. S. Harilal, D. Campos, and A. Hassanein, J. Appl. Phys. **108**, 063306 (2010).

[18] S. S. Harilal, B. O'Shay, M. S. Tillack, and M. V. Mathew, J. Appl. Phys. **98**, 013306 (2005).

[19] H. Lan, H. Lei, D. Zuo, X. Wang, and G. Zheng, Vacuum **135**, 86 (2017).

[20] J. Iqbal, R. Ahmed, M. Rafique, M. Anwar-ul Haq, and M. A. Baig, Laser Phys. **26**, 076001 (2016).

[21] S. Namba, S. Fujioka, H. Sakaguchi, H. Nishimura, Y. Yasuda, K. Nagai, N. Miyanaga, Y. Izawa, K. Mima, K. Sato *et al.*, J. Appl. Phys. **104**, 013305 (2008).

[22] E. R. Kieft, J. J. A. M. van der Mullen, G. M. W. Kroesen, V. Banine, and K. N. Koshelev, Phys. Rev. E **70**, 066402 (2004).

[23] A. Kramida, Yu. Ralchenko, J. Reader, and NIST ASD Team, *NIST Atomic Spectra Database (version 5.5.6)* (National Institute of Standards and Technology, Gaithersburg, MD, 2018); available at: https://physics.nist.gov/asd.

[24] C. Moore, *Atomic Energy Levels* (National Bureau of Standards, Gaithersburg, MD, 1958), Vol. III.

[25] J. Reader, C. H. Corliss, W. L. Wiese, and G. A. Martin, *Wavelengths and Transition Probabilities for Atoms and Atomic Ions*, Part. I. Wavelengths, Nat. Stand. Ref. Data Ser., NSRDS-NBS 68 (US Government Printing Office, Washington, DC, 1980), p. 415.

[26] J. A. Carroll, Philos. Trans. R. Soc. A **225**, 357 (1926).

[27] K. R. Rao, Proc. Phys. Soc. **39**, 408 (1926).

[28] R. C. Gibbs, A. M. Vieweg, and C. W. Gartlein, Phys. Rev. **34**, 406 (1929).

[29] R. J. Lang, Phys. Rev. **35**, 445 (1930).

[30] A. N. Ryabtsev, S. S. Churilov, and É. Y. Kononov, Opt. Spectr. (USSR) **100**, 652 (2006) [English translation].

[31] C.-M. Wu, Master's thesis, University of British Columbia (1967).

[32] E. H. Pinnington, J. A. Kernahan, and W. Ansbacher, Can. J. Phys. **65**, 7 (1987).

[33] J. A. Kernahan, E. H. Pinnington, W. Ansbacher, and J. L. Bahr, Nucl. Instr. Methods Phys. Res. B **9**, 616 (1985).

[34] T. Andersen, A. K. Nielsen, and G. Sørensen, Phys. Scr. **6**, 122 (1972).

[35] V. Kaufman, J. Sugar, T. A. M. Van Kleef, and Y. Joshi, J. Opt. Soc. Am. A **2**, 426 (1985).

[36] P. Dunne and G. O'Sullivan, J. Phys. B **25**, L593 (1992).

[37] A. N. Ryabtsev, S. S. Churilov, and É. Y. Kononov, Opt. Spectr. (USSR) **102**, 354 (2007) [English translation].

[38] M. A. Lysaght, D. Kilbane, A. Cummings, N. Murphy, P. Dunne, P. van Kampen, J. T. Costello, and E. T. Kennedy, J. Phys. B **38**, 4247 (2005).

[39] M. Lysaght, D. Kilbane, N. Murphy, A. Cummings, P. Dunne, and G. O'Sullivan, Phys. Rev. A **72**, 014502 (2005).

[40] U. I. Safronova, I. M. Savukov, M. S. Safronova, and W. R. Johnson, Phys. Rev. A **68**, 062505 (2003).

[41] E. P. Ivanova, At. Data Nucl. Data Tables **97**, 1 (2011).

[42] X.-B. Ding, F. Koike, I. Murakami, D. Kato, H. A. Sakaue, C.-Z. Dong, and N. Nakamura, J. Phys. B **45**, 035003 (2012).

[43] J. Grumer, R. Zhao, T. Brage, W. Li, S. Huldt, R. Hutton, and Y. Zou, Phys. Rev. A **89**, 062511 (2014).

[44] K.-T. Cheng and Y.-K. Kim, J. Opt. Soc. Am. **69**, 125 (1979).

[45] D. Kurilovich, A. L. Klein, F. Torretti, A. Lassise, R. Hoekstra, W. Ubachs, H. Gelderblom, and O. O. Versolato, Phys. Rev. Appl. **6**, 014018 (2016).

[46] W. F. Meggers, J. Res. Natl. Bur. Stand. **24**, 153 (1940).

[47] K. Haris, A. Kramida, and A. Tauheed, Phys. Scr. **89**, 115403 (2014).

[48] K. Haris and A. Tauheed, Phys. Scr. **85**, 055301 (2012).

[49] T. A. M. Van Kleef and Y. N. Joshi, Phys. Scr. **24**, 557 (1981).

[50] A. N. Ryabtsev, S. S. Churilov, and E. Y. Kononov, Phys. Scr. **72**, 377 (2005).

[51] B. Edlén, in *Spektroskopie I (Handbuch der Physik)* (Springer, Berlin, 1964), pp. 80–220.

[52] R. D. Cowan, *The Theory of Atomic Structure and Spectra*, modified by A. Kramida (University of California Press, Berkeley, 1981).

[53] A. Kramida, Comput. Phys. Commun. **182**, 419 (2011).

[54] C. J. Sansonetti, Fortran computer code POLAR (private communication, 2005).

[55] J. Sucher, Phys. Rev. A **22**, 348 (1980).

[56] Y. Ishikawa, R. Baretty, and R. C. Binning Jr., Chem. Phys. Lett. **121**, 130 (1985).

[57] E. Eliav, M. J. Vilkas, Y. Ishikawa, and U. Kaldor, J. Chem. Phys. **122**, 224113 (2005).

[58] G. L. Malli, A. B. F. Da Silva, and Y. Ishikawa, Phys. Rev. A **47**, 143 (1993).

[59] E. Eliav, U. Kaldor and Y. Ishikawa (with contributions by A. Landau), *TRAFS-3C Code (Tel-Aviv Relativistic Atomic Fock-Space Coupled Cluster Code)* (1990–2013).

[60] V. M. Shabaev, I. I. Tupitsyn, and V. A. Yerokhin, Comput. Phys. Commun. **189**, 175 (2015).

[61] J. C. Berengut, V. V. Flambaum, and M. G. Kozlov, Phys. Rev. A **73**, 012504 (2006).

[62] J. C. Berengut, Phys. Rev. A **84**, 052520 (2011).

[63] J. C. Berengut, Phys. Rev. A **94**, 012502 (2016).

[64] E. V. Kahl and J. C. Berengut, arXiv:1805.11265.